Link between superconductivity and a Lifshitz transition in intercalated math xmlns="http://www.w3.org/1998/Math/MathML">msub>mi mathvariant="normal">Bi/mi>mn>2/mn>/msub>msub>mi mathvariant="normal">Se/mi>mn>3/mn>/msub>/math>

A. Almoalem, I. Silber, S. Sandik, M. Lotem, A. Ribak, Y. Nitzav, A. Yu. Kuntsevich, O. A. Sobolevskiy, Yu. G. Selivanov, V. A. Prudkoglyad, M. Shi, L. Petaccia, M. Goldstein, Y. Dagan, and A. Kanigel

Phys. Rev. B **103**, 174518 — Published 26 May 2021

DOI: 10.1103/PhysRevB.103.174518

Link between superconductivity and a Lifshitz transition in intercalated Bi_2Se_3

A. Almoalem,[1] I. Silber,[2] S. Sandik,[2] M. Lotem,[2] A. Ribak,[1] Y. Nitzav,[1] A.Yu. Kuntsevich,[3] O.A. Sobolevskiy,[3] Yu.G. Selivanov,[3] V.A. Prudkoglyad,[3] M.Shi,[4] L. Petaccia,[5] M. Goldstein,[2] Y. Dagan,[2] and A. Kanigel[1]

[1] *Department of Physics, Technion – Israel Institute of Technology, Haifa, 32000, Israel*
[2] *School of Physics and Astronomy, Tel Aviv University, Tel Aviv, 6997801, Israel*
[3] *P.N. Lebedev Physical institute of the RAS, Moscow, 119991, Russia*
[4] *Swiss Light Source, Paul Scherrer Institut, CH-5232 Villigen, Switzerland*
[5] *Elettra Sincrotrone Trieste, Strada Statale 14 km 163.5, 34149 Trieste, Italy*

Topological superconductivity is an exotic phase of matter in which the fully gapped superconducting bulk hosts gapless Majorana surface states protected by topology. Intercalation of copper, strontium or niobium between the quintuple layers of the topological insulator Bi_2Se_3 increases the carrier density and leads to superconductivity that is suggested to be topological. Here we study the electronic structure of strontium-intercalated Bi_2Se_3 using angle resolved photoemission spectroscopy (ARPES) and Shubnikov-de Haas (SdH) oscillations. Despite the apparent low Hall number of $\sim 2 \times 10^{19}\mathrm{cm}^{-3}$, we show that the Fermi surface has a shape of an open cylinder with a larger carrier density of $\sim 10^{20}\mathrm{cm}^{-3}$. We suggest that superconductivity in intercalated Bi_2Se_3 emerges with the appearance of a quasi-2D open Fermi surface.

A promising avenue towards achieving topological superconductivity is to induce superconductivity in materials whose electronic structure is topologically nontrivial[1]. Intercalated Bi_2Se_3 has been suggested as a possible candidate for a topological superconductor based on the appearance of a zero-bias feature in the tunnelling conductance[2–5] and nematicity in the superconducting state[5–12]. A possible explanation to the zero bias peak is the existence of Majorana modes[2,4,5]. Also, nematicity can be accounted for by a two-component Ginzburg-Landau theory with nematic solutions corresponding to topological-superconductivity with odd-parity E_u symmetry (the order parameter is odd under the operation $\mathrm{x} \to -\mathrm{x}$ and $\mathrm{y} \to -\mathrm{y}$). Such nematic solutions require an open, quasi-2D, Fermi-Surface[13–16].

A simple criterion has been put forth for determining whether superconductivity in Bi_2Se_3-derived systems is 3D topological time-reversal-invariant (TRI): the Fermi surface (FS) has to enclose an odd number of time-reversal-invariant-momenta (TRIM) points[17]. Superconducting $A_xBi_2Se_3$ compounds are slightly electron-doped ($n \sim 10^{19} - 10^{20}$ cm^{-3}) with the bottom of the conduction band located at the center of the Brillouin zone[18]. In $Cu_xBi_2Se_3$, ARPES, Shubnikov-de Hass (SdH) and de Haas-van Alphen[19,20] experiments found an open FS that encloses two TRIM points (Γ and Z) thus not fulfilling the aforementioned criterion but suggesting the possibility of weak 2D topological superconductivity.

Increasing the carrier density of Bi_2Se_3 via Cu intercalation results in a quick expansion of the FS towards the Z point and eventually a Lifshitz transition into an open cylindrical-like FS[19]. Interestingly, Sr intercalated Bi_2Se_3 is reported to have an order of magnitude smaller carrier concentration as compared to the Cu intercalation, while still exhibiting superconductivity with similar critical temperature T_c[7,21,22]. This raises two questions: 1) Does $Sr_xBi_2Se_3$ have a closed Fermi surface that allows for a 3D topological TRI superconductivity? 2) How can such a small amount of carriers produce a $T_c \simeq 3$K?

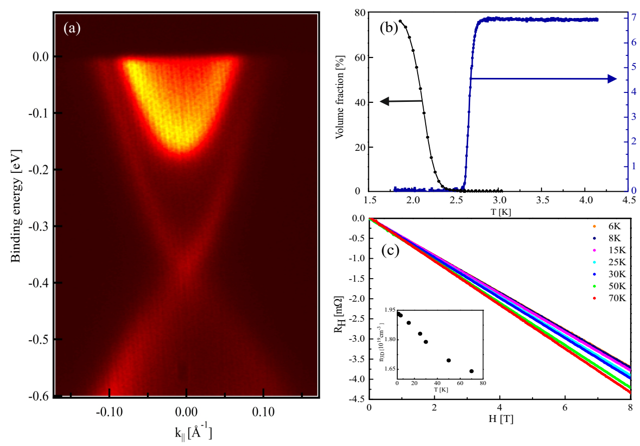

FIG. 1. Bulk superconductivity coexists with topological surface states in $Sr_xBi_2Se_3$. (a) Typical ARPES spectra, taken using a 20 eV photon energy at $T = 28.5$ K, displays the electron-like band and the surface states. The Dirac point lies about 375 meV below the Fermi-level. (b) Resistance and magnetization measurements of the sample measured in the Shubnikov-de-Hass part. The sharp resistive transition at 2.7K, along with the large superconducting volume fraction, clearly demonstrate a 3D bulk superconductivity. (c) Hall measurements at various temperatures. The linearity of the Hall coefficient with respect to the magnetic field is visible, while a clear temperature dependence is apparent. Inset: The carrier density inferred from the Hall measurements vs. temperature.

In this paper we combine the SdH effect and ARPES measurements to determine the shape of the Fermi-surface, motivated by the relatively small Hall number of $Sr_xBi_2Se_3$. We study $Sr_xBi_2Se_3$ samples with $x_{nominal} = 0.15$, crystal growth and chracterization are described in Ref.[7,23] and in appendix A. The samples display Dirac-like surface states as well as a parabolic bulk band. A naive estimate of the carrier density from the Hall slope yields a carrier concentration of $\sim 2 \times 10^{19}\mathrm{cm}^{-3}$. This estimate is in good agreement with the binding-energy of the Dirac-point[19], but has a noticeable temperature dependence (see Fig.1). Bulk superconductivity is evident from the large SC volume fraction, which extrapolates to 100% at zero temperature, with $T_c = 2.7$K.

The frequency of the resistance-oscillations as a function of inverse magnetic field corresponds to the cross-sectional areas of the extrema of the FS perpendicular to the magnetic field[24]. We therefore rotate the magnetic field with respect to the c-axis (θ) to resolve the shape of the FS. Our main finding using this method is the clear observation of two frequencies when the magnetic field is parallel to the c-axis, $\theta = 0$ (see Fig. 2(a)).

This finding is a strong evidence for an open FS, as two frequencies will only show up if the FS have two extrema with different cross-sectional area. Therefore, A closed Fermi-surface would have two frequencies only for a complicated shape, which is inconsistent with previous ARPES measurements and theoretical DFT and $k \cdot p$ calculations[18,25].

The two frequencies persist over a wide temperature range. However, as we increase θ only one frequency remains visible in the SdH data beyond 10°. The remaining frequency increases when rotating the field away from the c-axis, becoming unresolved for $\theta >$57°. This frequency is well described by $1/\cos(\theta)$, as expected for an open cylindrical-type FS (see Fig. 2). A possible explanation for the rapid disappearance of the second frequency is a field assisted tunneling between adjacent semi-classical orbits, similar to the magnetic breakdown phenomena[26,27]. To account for the decrease in the higher frequency, we have to assume a rather sharp corrugation on top of an open cylindrical-like Fermi surface. This FS results in two semi classical orbits that are separated in the kz direction, but the shorter one spans a larger portion of the Brillouin zone. At an out-of-plane magnetic field the Lorentz force is confined in-plane, but upon increasing the tilt angle, the Lorentz force acquires a k_z component, allowing the semi-classical electron to scatter to the shorter orbit. Furthermore, the tilting of the magnetic field brings the two semi classical orbits closer in k space, making the tunnelling between the orbits even more probable.

Due to the larger uncertainties for $\theta > 50°$, we found it necessary to support our analysis suggesting an open FS in $\mathrm{Sr_xBi_2Se_3}$. We turn to ARPES measurements in which we vary the photon energy and thus scan the entire Brillouin zone along the k_z direction[19,28,29]. The inner-potential that determines the conversion of photon-energy to momentum normal-to-the-surface is derived in appendix E.

Each panel in Fig. 3 displays the dispersion of the conduction band with respect to the momentum parallel to the surface for different photon energies. We find intensity corresponding to the bulk band for all measured k_z values, including the Γ and Z points. Our data show-

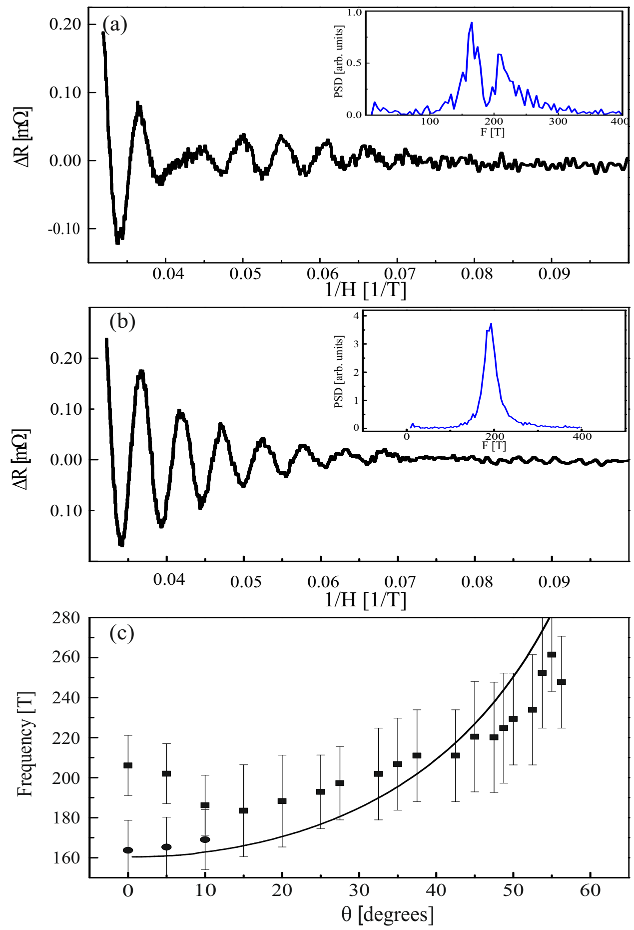

FIG. 2. Angular dependence of the SdH frequency at 0.4 K. (a) Two frequencies are observed for $\theta \simeq 0°$. The two frequencies point to an open Fermi surface as explained in the text. (b) As we rotate the sample to larger out of plane angles, we observe only one frequency above a certain angle, as can be seen, for example, at $\theta \simeq 20°$. (c) SdH frequency as a function of angle. The solid line represent the expected angular dependence of one SdH frequency for an open cylinder. The insets in (a) and (b) are the Fourier power spectrum of the quantum oscillations vs inverse magnetic field (1/H). θ is the angle between the magnetic field direction and the c-axis.

ing finite density of states at both Z-points support our conclusion of open FS. For comparison, we note that no intensity is seen by ARPES at the k_z corresponding to the Z points for low carrier density samples of $\mathrm{Bi_2Se_3}$ having a closed FS[19,30]. The bandwidth changes with k_z and is maximal at the Γ-point, similarly to the case of $\mathrm{Cu_xBi_2Se_3}$ and consistent with our SdH data. Furthermore, the Fermi-momentum is independent of k_z, suggesting a nearly perfect cylinder. The constant Fermi-momentum in the $k_x - k_y$ plane for different k_z suggests that the effective mass of the band depends on k_z (see appendix G).

The temperature and intercalation dependence of the Hall coefficient casts a doubt whether it can be used for an accurate determination of the carrier density. The

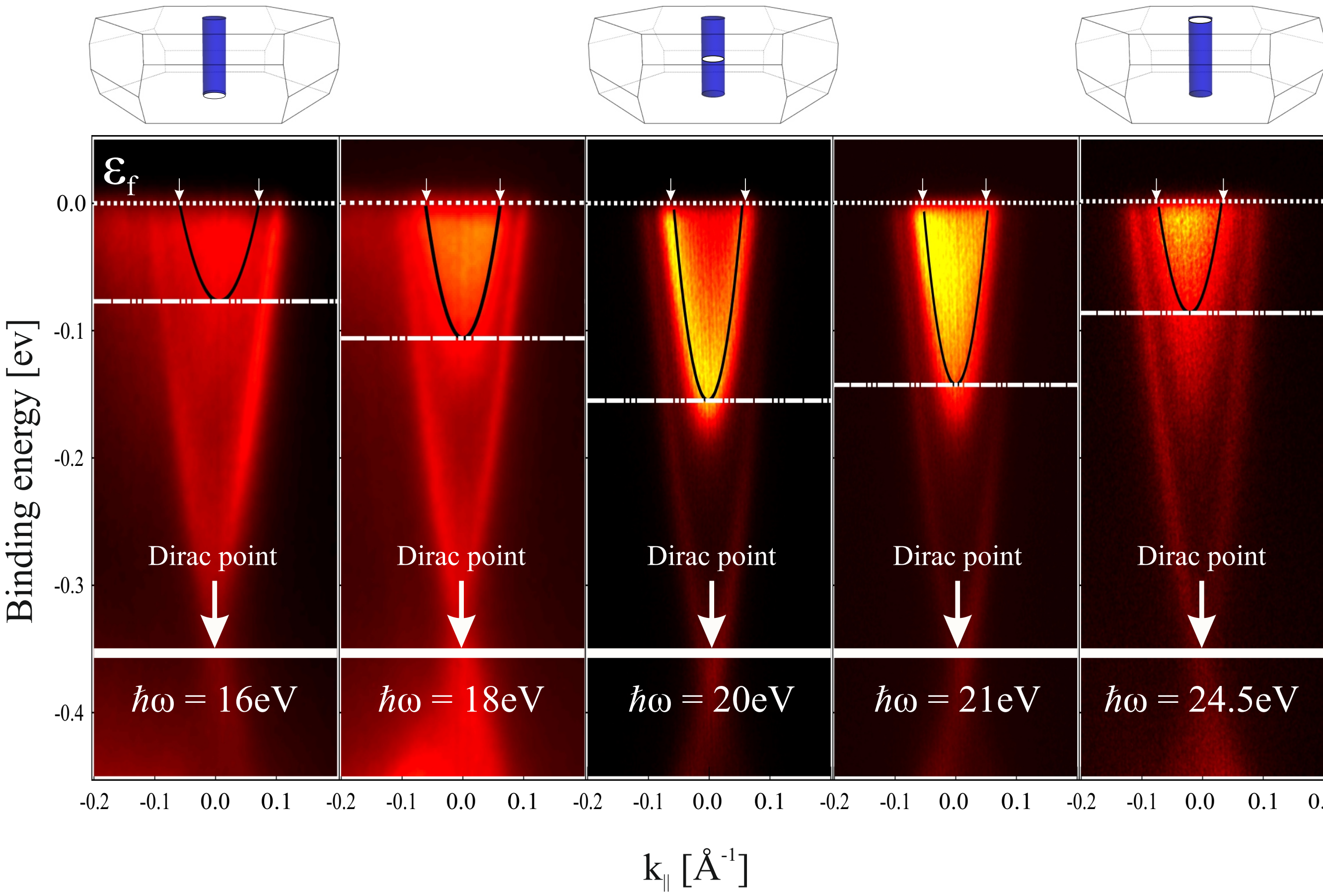

FIG. 3. Band structure of $Sr_xBi_2Se_3$ samples measured at various photon energies, each photon energy corresponds to a different k_z value (see appendix E). The two outmost panels are measurements at the two Z points, while the middle panel is a measurement at k_z=0. The 16 and 18 eV data were measured at the BaDElPh beam line at Elettra, and the 20, 21, 24.5 eV data were measured at the SIS beamline at the SLS,PSI. The small arrows mark the Fermi momentum, and the large arrow marks the Dirac point. The Fermi-level and the minimum of the band are marked by dashed and dashed-dotted lines, respectively. In all panels the energy of the Dirac point is the same, as expected. Drawings on top: An illustration of the constant k_z plane at which the spectra in the panel below it was measured.

Hall number is almost independent of Sr intercalation, albeit this intercalation is the main mechanism for doping mobile electrons in the sample[23,31]. Together with the unexpected large temperature dependence of the Hall number we conclude that the Hall-inferred density is unreliable. Doped Bi_2Se_3 has a single parabolic band close to the Fermi-energy, and if we assume that the SdH signal originates only from the conducting bulk, the interpretation of the data is straightforward and gives an exact information about the volume of the Fermi-surface and the carrier density. We therefore revisit our previous results and calculate the carrier density from the volume in momentum space as inferred from ARPES and SdH. The Fermi momentum from the ARPES, yields $n = 6.5 \pm 1 \times 10^{19}$ cm^{-3} for a non corrugated cylinder. The SdH numbers for this sample and for other samples are summarized in Table I.

A similar Fermi-surface topology is found in *all* intercalated Bi_2Se_3 samples exhibiting superconductivity[19,32]. This observation raises the question of why does superconductivity appear concomitantly with an open Fermi-surface?

Intuitively, one might expect that the opening of the FS will result in a quasi-2D band structure that has a larger density of states compared with the 3D case, for same carrier density. In the framework of weak-coupling BCS theory, the increase in density of states would enhance the critical temperature T_c. We use a simple model to quantify this intuitive idea, using weak-coupling limit BCS theory and the band-structure of Bi_2Se_3, based on DFT calculations for pure Bi_2Se_3[2,33]. To account for the effect of the intercalation the coupling amplitudes in the $\hat{z}$ direction are varied as a function of the chemical potential[25]. The FS of this band-structure is a narrow ellipsoid *closed* surface at low carrier densities and a cylindrical *open* surface at high carrier densities, as shown in Fig. 4, and in agreement with the experimental observation.

We can gauge the effect of the Lifshitz transition by plugging the density of states $g(\mu)$ into the standard weak coupling BCS[34] expression for the critical temperature T_c in the weak coupling regime:

$$k_B T_c \approx 1.14\hbar\omega_D \exp\left(-\frac{1}{V \cdot g(\mu)}\right), \quad (1)$$

where ω_D is the Debye frequency and V is the electron-phonon coupling constant. We use the known ω_D and adjust V to match the critical temperature of the system at large enough carrier densities where $g(\mu)$ is approximately constant. Assuming that V is independent of carrier density, we can plug it back into Eq. (1) and estimate T_c for different carrier densities. As shown in Fig. 4, the critical temperature of the open FS ($n > 5 \times 10^{19}\text{cm}^{-3}$) is approximately constant, but drops sharply at carrier densities below the Lifshitz transition once the Fermi surface closes. Two experimental points $T_c(n)$ are indicated on the plot, matching the critical temperatures and carrier densities for $Cu_xBi_2Se_3$ and $Sr_xBi_2Se_3$ deduced from SdH measurements.

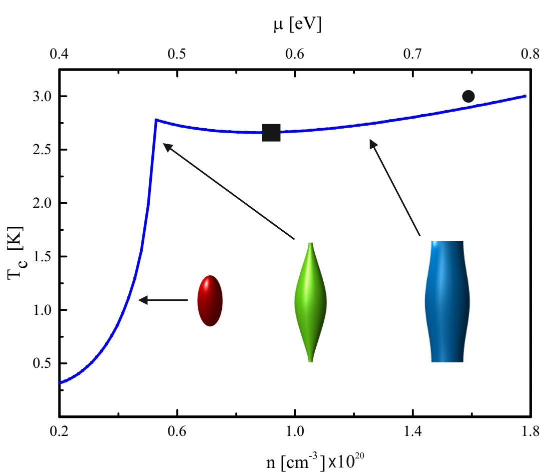

FIG. 4. Theoretical chemical potential/carrier density dependence of the superconducting critical temperature, obtained by combining DFT-based band structure with the BCS theory. Note the chemical potential calculated is about 3 times larger compared to the maximum bandwidth obtaines by ARPES. Two experimental points are presented, a black dot for $Cu_xBi_2Se_3$[19] and a black square for $Sr_xBi_2Se_3$, showing the consistency of the theoretical model.

The main finding is that superconducting samples always have large ($\geq 6.5\times10^{19}\text{cm}^{-3}$) carrier density, which results in an open FS, consistent with our simplified model and measurements done using different techniques. From the theoretical point of view[17], a 3D topological superconductor is not achievable with our suggested Fermi-surface. This still leaves the door open for other scenarios of weak 2D topological superconductivity[35].

Sample	n_{SdH} cm^{-3}	n_{Hall} cm^{-3}	ref.
Bi_2Se_3 (not SC)	1.9×10^{18}	3.7×10^{17}	19
Bi_2Se_3 (not SC)	1.8×10^{19}	2.3×10^{19}	19
$Cu_xBi_2Se_3$ (SC)	1.6×10^{20}	2.7×10^{20}	19
$Sr_xBi_2Se_3$ (SC)	9.3×10^{19}	$2\times10^{19*}$	This paper

TABLE I. Comparison between the Hall carrier density and the SdH carrier density. * - The Hall density of $Sr_xBi_2Se_3$ is taken at $T = 6$ K.

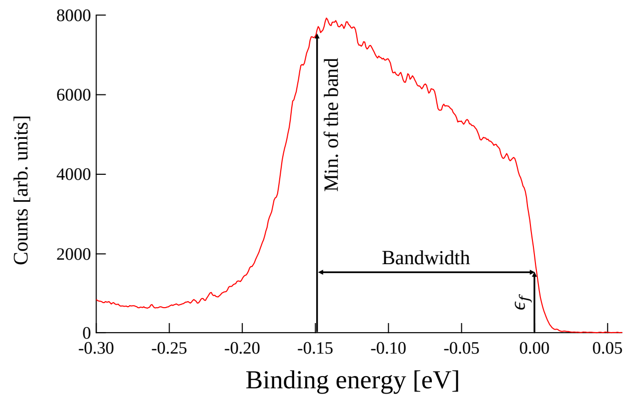

FIG. 5. EDC at $k_{||} = 0$ (Γ point) used to identify the Fermi energy. The exponential-like increase of the counts is observed at the energy range -0.25 to -0.15 eV. We define the bandwidth as the energy difference between the end of the exponential-like increase and the Fermi level.

An open Fermi-surface is consistent with two more observations. First, the most realistic physical mechanism of superconducting pairing in $Sr_xBi_2Se_3$ is the electron-phonon interaction, that occurs at small phonon momenta[14,36]. An open Fermi-surface allows this mechanism to be energetically favourable[14], as confirmed recently by inelastic neutron scattering[37]. Second, as shown in Ref.[38], for an odd-parity E_u pairing, the nodeless superconducting gap observed in tunnelling measurements in $Cu_xBi_2Se_3$[2,4,5] and Sr_xBi_2Se[39] is consistent only with an open Fermi-surface.

In addition, the suggested mean-field picture with the very weak dependence of T_c on the density is in agreement with the observation of a Hall density independent T_c in Cu-co-doped $Sr_xBi_2Se_3$ crystals[22].

Finally, we note that according to our simplified model a small region in the carrier density (4-5$\times10^{19}$ cm^3) - temperature phase diagram may allow for a 3D topological superconductivity. This would require precise tuning of carrier density, possibly using gate voltage or proper co-doping.

I. ACKNOWLEDGMENTS

A. Almoalem and I. Silber contributed equally to this work. ARPES experiments were conducted at the Surface/Interface Spectroscopy (SIS) beamline of the Swiss Light Source at the Paul Scherrer Institut in Villigen, Switzerland and at the BaDElPh beamline of Elettra. The high magnetic field measurements were performed at the National High Magnetic Field Laboratory, which is funded by the National Science Foundation through DMR-1157490 and the U.S. Department of Energy and the State of Florida. The work on the Russian site (crystal growth and magnetotransport measurements) was supported by the Russian Science Foundation (Grant No. 17-12-01544). Magnetotransport measurements were performed using the equipment of the LPI shared facility center. Work at Tel Aviv University and at the Technion is supported by the Israeli Science Foundation under grant number 382/17 and 320/17 respectively. Theoretical work is supported by Israel Science Foundation (Grant No. 227/15), US-Israel Binational Science Foundation (Grant No. 2016224). We acknowledge useful discussions with Assa Auerbach.

Appendix A: Sample preparation

Our samples are single crystals grown using the modified Bridgeman method. Elemental Bi, Se and Sr were loaded in quartz ampules in a glove box with an inert environment, and sealed in an evacuated tubes. More details on the growing process is described elsewhere[7,23]. Samples with lateral dimensions $0.5-5$ mm^2 were cleaved from the boule. All samples have full volume fraction as measured by magnetization curves (see Fig. 1(b) in main text), the data taken down to 1.7 K, where the volume fraction is ≈ 70 % as expected from previous measurements. Extrapolating the data down to 0 K gives a volume fraction of 100%. Resistivity measurements gives $T_C = 2.77$ K as defined by the onset of the transition, with a width of ≈ 0.2 K[7]. We denote the nominal Sr content x_{nominal}, because its real content (~ 0.06) is systematically smaller than the nominal value (in our case 0.15)[31].

The crystals were previously shown to consist of blocks (with dimensions of several hundred μm)with slight mutual misorientation[7]. Since the properties of the neighboring blocks may slightly vary, for magnetooscillation studies done at the Russian site we cleaved as small blocks as possible and glued the contacts with a silver paint. The blocks were cleaved along the basal plane and had mirror-like top and bottom surfaces. Magnetooscillaion studies done at the National High Magnetic Field Laboratory in Florida were done using cured silver epoxy contacts with Pt wires.

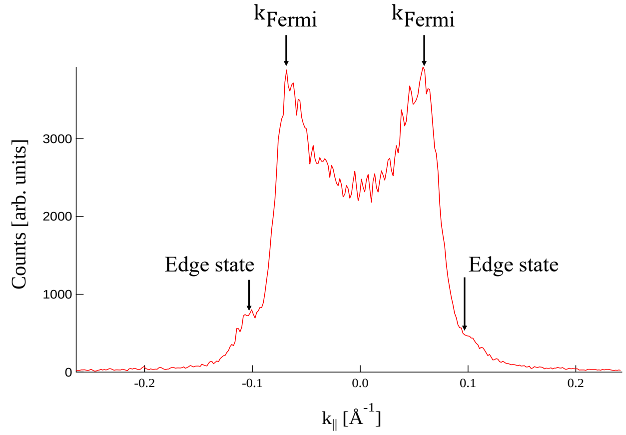

FIG. 6. Momentum dispersive curve taken at the Fermi level. The Fermi momentum points are marked by arrows. Also marked are the edge states, with a lower counts than the bulk band.

Appendix B: ARPES measurements

ARPES measurements were done at the SIS beamline at the SLS in the Paul Scherrer Institute (Switzerland) and at BaDElPh beamline at Elettra (Italy). Samples at the SLS were cleaved and measured at $T = 12$ K and in vacuum better than 5E-11 torr, with photon energy increments of 0.5 eV, ranging from 20 to 35 eV. Samples at Elettra were cleaved and measured at $T = 28.5$ K and in vacuum better than 5E-11 torr, with photon energy increments of 0.5 eV, ranging from 15 to 24 eV. The energy resolution is ~ 10 meV.

Appendix C: Transport measurements

R(T) measurements were done in an home-built He_4 cryostat, with electrical current of 0.5 mA. Keithley 6221 supplied the current and the voltage drop was recorded with a Keithley 2182A nanovoltmeter in the delta mode configuration. Hall measurements were measured in a Quantum Design PPMS using the same delta mode configuration, while applying a larger current of 1 mA. The data is presented after averaging two perpendicular R_{xy} configurations and symmetrization in respect to positive and negative applied magnetic fields.

The high fields measurements were taken in a wet He_3 cryostat at the National High Magnetic Field Laboratory (NHMFL) in Tallahassee, Florida. The maximum field of 31 Tesla was ramped up in a typical scan rate of 1.5 Tesla per minute. Resistance was measured using a Lakeshore 372 resistance bridge with current of 316 μA. The out of plane angle was determined by the brushless stepper motor encoder, while keeping the sweep direction constant in order to avoid any mechanical back-slash. The stepper motor and rotator platform were tested the day prior to the measurements by measuring the critical field of a 2D

FIG. 7. A fit of the Brillouin zone high symmetry points locations, Γ and Z, to the photon energy. Using the free electron final state approximation we extract the inner potential, $V_0 \approx 10$ V, and map all of the scans to their respective k_z values. The red line is the fit using the extracted inner potential, the blue points with the error bars represents the locations of the Γ and Z points and the uncertainty in photon energy and k_z value.

superconducting $4H_b - TaS_2$ sample in different angles.

Appendix D: Band dispersion determination

We define the bottom of the band as a point were an exponential-like increase of intensity intersects with a linear trend of the intensity. We use an average of 6 energy dispersive curves (EDC's) located around $k_{||} = 0$ (Fig. 5). We define the Fermi momentum as a start of a prominent decrease in intensity, when diverging from $k_{||} = 0$ towards higher absolute values of $k_{||} = 0$ (Fig. 6). This is done using a momentum dispersive curve (MDC) located slightly below the Fermi energy ($E \sim E_f$).

Appendix E: Band dispersion along k_z

To resolve k_z values we use the free-electron final state approximation[19,29,40]: $k_z = \sqrt{2m^*/\hbar^2(E_{kin} + V_0)}$. The mapping of band dispersion in the k_z direction is then carried out by changing the photon energy used in the photoemission process, thus changing the value of E_{kin} and obtaining a different value for k_z. The constant V_0 is specific to the material and is called the inner potential, formally it is given by $V_0 = \mu + \phi$, where μ is the chemical potential measured from the bottom of the band and ϕ is the work function. By fitting the photon energies of the high symmetry points of the Brillouine zone (Γ and Z) and using the known values of k_z for those points, we can extract the inner-potential. In Figure 7 we plot the position of the high-symmetry points as a function of photon energy, and obtain a value of approximately $V_0 \sim 10$eV .

Appendix F: Theoretical calculations of the BCS model

The calculation of the Fermi surface and the electronic density of states (DOS) is based on an effective tight-binding low-energy Hamiltonian obtained for clean Bi_2Se_3 from DFT calculations[2,33], introducing a chemical potential dependence in several of the parameters in order to account for intercalation effects[25]. The Hamiltonian in eq. F1 is taken according to the supplemental of Ref.[2]:

$$
\begin{aligned}
H(\boldsymbol{k}) &= \begin{pmatrix} \varepsilon(\boldsymbol{k}) + M(\boldsymbol{k}) & & A_1(\boldsymbol{k}) & A_2(\boldsymbol{k}) \\ & \varepsilon(\boldsymbol{k}) + M(\boldsymbol{k}) & A_2^*(\boldsymbol{k}) & -A_1(\boldsymbol{k}) \\ A_1(\boldsymbol{k}) & A_2(\boldsymbol{k}) & \varepsilon(\boldsymbol{k}) - M(\boldsymbol{k}) & \\ A_2^*(\boldsymbol{k}) & -A_1(\boldsymbol{k}) & & \varepsilon(\boldsymbol{k}) - M(\boldsymbol{k}) \end{pmatrix}, \qquad \text{(F1)} \\
\varepsilon(\boldsymbol{k}) &= -\mu + \bar{D}_1(2 - 2\cos(k_z c)) + \frac{4}{3}\bar{D}_2\left(3 - 2\cos\left(\frac{\sqrt{3}}{2}k_x a\right)\cos\left(\frac{1}{2}k_y a\right) - \cos(k_y a)\right), \\
M(\boldsymbol{k}) &= M_0 - \bar{B}_1(2 - 2\cos(k_z c)) - \frac{4}{3}\bar{B}_2\left(3 - 2\cos\left(\frac{\sqrt{3}}{2}k_x a\right)\cos\left(\frac{1}{2}k_y a\right) - \cos(k_y a)\right), \\
A_1(\boldsymbol{k}) &= \bar{A}_1 \sin(k_z c), \\
A_2(\boldsymbol{k}) &= \frac{2}{3}\bar{A}_2\left(\sqrt{3}\sin\left(\frac{\sqrt{3}}{2}k_x a\right)\cos\left(\frac{1}{2}k_y a\right) + i\left[\cos\left(\frac{\sqrt{3}}{2}k_x a\right)\sin\left(\frac{1}{2}k_y a\right) + \sin(k_y a)\right]\right).
\end{aligned}
$$

We take $a = 4.14$ Å, and note that here $c = 9.58$Å is the height of the primitive unit cell, and not of the hexagonal lattice as often appears in the literature. For a chemical potential $\mu = 0.4$eV the coefficients are taken as in[2]. Intercalation is expected to mostly affect the parameters characterizing the k_z dependence, namely $\bar{D}_1, \bar{B}_1, \bar{A}_1$. Thus, these components are chosen for $\mu = 0.65$eV as in Ref.[25], and interpolated linearly in between. For the convenience of the reader we list the values of all the parameters in Table II. Note that the qualitative behavior of the results is not sensitive to this interpolation.

Diagonalizing the Hamiltonian results in two spin-degenerate bands, with the chemical potential in the gap between them:

$$\xi_{\pm}\left(\boldsymbol{k}\right)=\varepsilon\left(\boldsymbol{k}\right)\pm\sqrt{M^{2}\left(\boldsymbol{k}\right)+A_{1}^{2}\left(\boldsymbol{k}\right)+\left|A_{2}\left(\boldsymbol{k}\right)\right|^{2}}. \tag{F2}$$

Intercalation raises the carrier density and shifts the chemical potential into the (twofold degenerate) upper band $\xi_{+}\left(\boldsymbol{k}\right)$. The carrier density at the Fermi energy μ is then given by

$$n\left(\mu\right)=2\int_{BZ}\frac{d^{3}k}{\left(2\pi\right)^{3}}\Theta\left(-\xi_{+}\left(\boldsymbol{k}\right)\right). \tag{F3}$$

Holding all parameters (including $\bar{D}_1, \bar{B}_1, \bar{A}_1$) constant for each μ, we can numerically differentiate $n\left(\mu\right)$ and obtain the DOS $g\left(\mu\right)$, which we then plug into the BCS formula.

Appendix G: Additional data

Additional SdH data measured on a different sample from the same growth as described in the main text and also for the sample with nominal composition $Sr_{0.1}Bi_2Se_3$. The resutls for different samples were similar. SdH oscillations in magnetic fields up to 16 T are observed up to $\theta\approx 55°$ (see Fig. 8(a)). Due to lower available magnetic field, an FFT procedure was replaced with a minima-maxima counting procedure to evaluate the frequency at each angle (Fig. 8(b)), the linear relation observed between the order of the maxima to $1/H$, clearly shows the strength of this procedure, although it obscures the two frequencies observed at low angles. This data analysis reinforced our conclusion of an open FS in these samples based on the fit of the results to the known $1/cos(\theta)$ relation for an open-cylindrical FS (Fig. 8(c)). The dingle plot presented in Fig. 8(d) gives an averaged effective mass with excellent agreement to the results acquired from the ARPES data (Fig. 9).

Summary of all the ARPES data from both the sample from PSI (blue) and at Elettra (red) is presented in Fig. 9. The data spans about two Brillouin zones clearly show that an open FS is measured, as a finite bandwidth is visible at every scan. Figure 9(a) shows the bottom of the band as function of k_z. A clear change in the bottom of the band, with values ranging from ~ 150 meV at the Γ point, to ~ 80 meV at the edge of the Brillouin zone (Z point) is shown. Each photon energy is a cut at different k_z, thus a closed FS would have zero intensity at the edge of the Brillouin zone.

Figure 9(b) shows the Fermi momentum as function of k_z. A constant Fermi momentum of $\sim k_{||}=0.062\pm 0.005$ Å^{-1} is observed at each k_z value indicating, an open cylinder-like FS. Due to the resolution, we were unable to determine if the FS is a perfect cylinder or a corrugated one, as implied by the SdH results. A cylindrical FS with a constant Fermi-Momentum suggests that the effective mass depends on k_z, as seen in Fig. 9(c). An open cylindrical FS with changing effective mass was seen previously in the closely related material, $Cu_xBi_2Se_3$[19].

<table>
<tr><th>μ</th><th>$\bar{D}_1$</th><th>$\bar{D}_2$</th><th>M_0</th><th>$\bar{B}_1$</th><th>$\bar{B}_2$</th><th>$\bar{A}_1$</th><th>$\bar{A}_2$</th></tr>
<tr><td>0.4</td><td>0.024</td><td rowspan="2">1.14</td><td rowspan="2">0.28</td><td>0.216</td><td rowspan="2">3.30</td><td>0.32</td><td rowspan="2">0.99</td></tr>
<tr><td>0.65</td><td>0.012</td><td>0.108</td><td>0.16</td></tr>
</table>

TABLE II. Model parameters (all in eV), taken from Refs.[2,25]

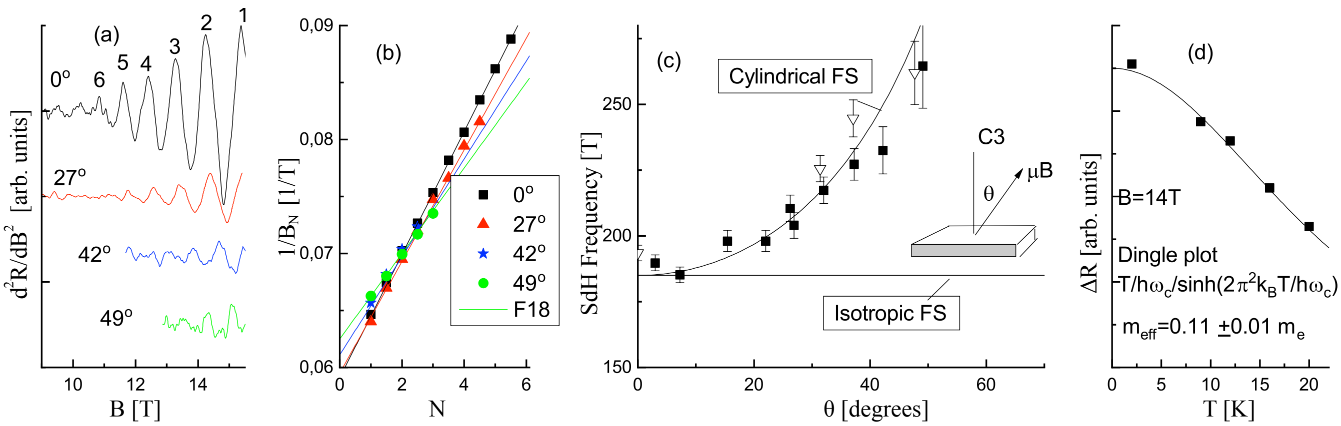

FIG. 8. (a) Shubnikov-de Haas oscillations for $Sr_{0.1}Bi_2Se_3$ taken for different θ. The maxima of oscillations ($\theta = 0$ case) are enumerated for frequency calculation; (b) Fan diagrams for the corresponding datasets from panel a); (c) Frequencies of the SdH oscillations versus tilt angle. The geometry of the experiment is shown in the panel. Lines show the expectations in two limits: cylindrical and spherical Fermi surfaces, respectively; (d) Temperature dependence of the Shubnikov-de-Haas oscillations amplitude at 14T (magnetic field is perpendicular to basal plane). Line is a fit with Lifshits-Kosevich formula(see text).

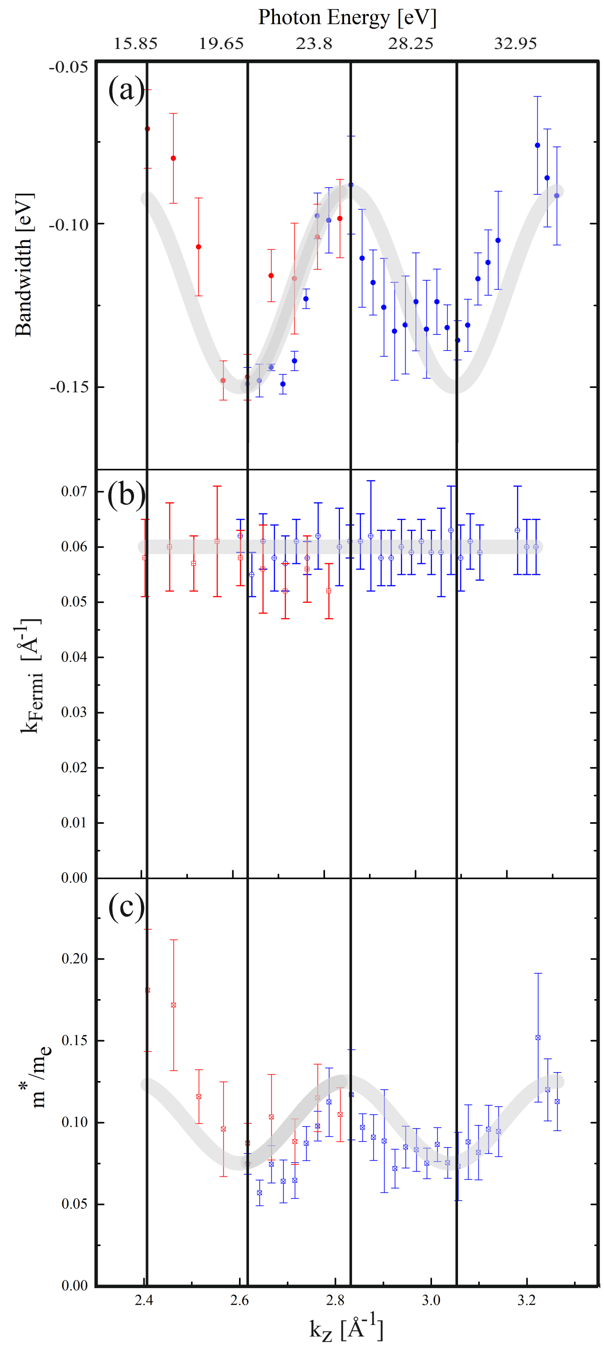

FIG. 9. Bandwidth (a), Fermi momentum (b) and relative effective mass (c) extracted for different k_z values on the $Z-\Gamma-Z$ line in the Brillouin zone, as described in the text. The k_z values were extracted using the inner potential and the free electron state approximation. The blue dots represnts data measured at PSI, on the same sample. Red dots represents data measured at Elettra on a different sample. An open Fermi surface is seen by the fact that the Fermi momentum is unchanged up to the Z point, and that the bandwidth is non-zero at every k_z value. Thick grey lines are guides to the eye.

[1] Y. S. Hor, A. J. Williams, J. G. Checkelsky, P. Roushan, J. Seo, Q. Xu, H. W. Zandbergen, A. Yazdani, N. P. Ong, and R. J. Cava, Physical review letters **104**, 057001 (2010).
[2] S. Sasaki, M. Kriener, K. Segawa, K. Yada, Y. Tanaka, M. Sato, and Y. Ando, Physical review letters **107**, 217001 (2011).
[3] T. Kirzhner, E. Lahoud, K. Chaska, Z. Salman, and A. Kanigel, Physical Review B **86**, 064517 (2012).
[4] N. Levy, T. Zhang, J. Ha, F. Sharifi, A. A. Talin, Y. Kuk, and J. A. Stroscio, Physical review letters **110**, 117001 (2013).
[5] R. Tao, Y.-J. Yan, X. Liu, Z.-W. Wang, Y. Ando, Q.-H. Wang, T. Zhang, and D.-L. Feng, Physical Review X **8**, 041024 (2018).
[6] K. Matano, M. Kriener, K. Segawa, Y. Ando, and G.-q. Zheng, Nature Physics **12**, 852 (2016).
[7] A. Y. Kuntsevich, M. Bryzgalov, V. Prudkoglyad, V. Martovitskii, Y. G. Selivanov, and E. Chizhevskii, New Journal of Physics **20**, 103022 (2018).
[8] A. Y. Kuntsevich, M. Bryzgalov, R. Akzyanov, V. Martovitskii, A. Rakhmanov, and Y. G. Selivanov, Physical Review B **100**, 224509 (2019).
[9] S. Yonezawa, K. Tajiri, S. Nakata, Y. Nagai, Z. Wang, K. Segawa, Y. Ando, and Y. Maeno, Nature Physics **13**, 123 (2017).
[10] K. Willa, R. Willa, K. W. Song, G. Gu, J. A. Schneeloch, R. Zhong, A. E. Koshelev, W.-K. Kwok, and U. Welp, Physical Review B **98**, 184509 (2018).
[11] Y. Sun, S. Kittaka, T. Sakakibara, K. Machida, J. Wang, J. Wen, X. Xing, Z. Shi, and T. Tamegai, Physical review letters **123**, 027002 (2019).
[12] T. Asaba, B. Lawson, C. Tinsman, L. Chen, P. Corbae, G. Li, Y. Qiu, Y. S. Hor, L. Fu, and L. Li, Physical Review X **7**, 011009 (2017).
[13] L. Fu, Physical Review B **90**, 100509 (2014).
[14] X. Wan and S. Y. Savrasov, Nature communications **5**, 4144 (2014).
[15] J. W. Venderbos, V. Kozii, and L. Fu, Physical Review B **94**, 180504 (2016).
[16] H. S. Røising, F. Flicker, T. Scaffidi, and S. H. Simon, Physical Review B **98**, 224515 (2018).
[17] L. Fu and E. Berg, Phys. Rev. Lett. **105**, 097001 (2010).
[18] W. Zhang, R. Yu, H.-J. Zhang, X. Dai, and Z. Fang, New Journal of Physics **12**, 065013 (2010).
[19] E. Lahoud, E. Maniv, M. S. Petrushevsky, M. Naamneh, A. Ribak, S. Wiedmann, L. Petaccia, Z. Salman, K. Chashka, Y. Dagan, *et al.*, Phys. Rev. B **88**, 195107 (2013).
[20] B. J. Lawson, G. Li, F. Yu, T. Asaba, C. Tinsman, T. Gao, W. Wang, Y. S. Hor, and L. Li, Physical Review B **90**, 195141 (2014).
[21] V. Maurya, P. Neha, P. Srivastava, S. Patnaik, *et al.*, Physical Review B **92**, 020506 (2015).
[22] A. Y. Kuntsevich, V. P. Martovitskii, G. V. Rybalchenko, Y. G. Selivanov, M. I. Bannikov, O. A. Sobolevskiy, and E. G. Chigevskii, Materials **12**, 3899 (2019).
[23] S. Volosheniuk, Y. G. Selivanov, M. Bryzgalov, V. Martovitskii, and A. Y. Kuntsevich, Journal of Applied Physics **125**, 095103 (2019).
[24] L. Onsager, The London, Edinburgh, and Dublin Philosophical Magazine and Journal of Science **43**, 1006 (1952).
[25] T. Hashimoto, K. Yada, A. Yamakage, M. Sato, and Y. Tanaka, Superconductor Science and Technology **27**, 104002 (2014).
[26] A. B. Pippard, Proceedings of the Royal Society of London. Series A. Mathematical and Physical Sciences **270**, 1 (1962).
[27] N. Harrison, J. Caulfield, J. Singleton, P. Reinders, F. Herlach, W. Hayes, M. Kurmoo, and P. Day, Journal of Physics: Condensed Matter **8**, 5415 (1996).
[28] S.-Y. Xu, Y. Xia, L. Wray, S. Jia, F. Meier, J. Dil, J. Osterwalder, B. Slomski, A. Bansil, H. Lin, *et al.*, Science **332**, 560 (2011).
[29] S. Hufner, *Photoelectron spectroscopy: principles and applications* (Springer Science & Business Media, 2013).
[30] Y. Tanaka, K. Nakayama, S. Souma, T. Sato, N. Xu, P. Zhang, P. Richard, H. Ding, Y. Suzuki, P. Das, *et al.*, Physical Review B **85**, 125111 (2012).
[31] Z. Liu, X. Yao, J. Shao, M. Zuo, L. Pi, S. Tan, C. Zhang, and Y. Zhang, Journal of the American Chemical Society **137**, 10512 (2015).
[32] B. Lawson, P. Corbae, G. Li, F. Yu, T. Asaba, C. Tinsman, Y. Qiu, J. E. Medvedeva, Y. S. Hor, and L. Li, Physical Review B **94**, 041114 (2016).
[33] H. Zhang, C.-X. Liu, X.-L. Qi, X. Dai, Z. Fang, and S.-C. Zhang, Nature physics **5**, 438 (2009).
[34] J. Bardeen, L. N. Cooper, and J. R. Schrieffer, Phys. Rev. **108**, 1175 (1957).
[35] L. Fu and C. L. Kane, Physical review letters **100**, 096407 (2008).
[36] P. Brydon, S. D. Sarma, H.-Y. Hui, and J. D. Sau, Physical Review B **90**, 184512 (2014).
[37] J. Wang, K. Ran, S. Li, Z. Ma, S. Bao, Z. Cai, Y. Zhang, K. Nakajima, S. Ohira-Kawamura, P. Čermák, *et al.*, Nature communications **10** (2019).
[38] L. Hao and C. Ting, Physical Review B **99**, 214507 (2019).
[39] G. Du, J. Shao, X. Yang, Z. Du, D. Fang, J. Wang, K. Ran, J. Wen, C. Zhang, H. Yang, *et al.*, Nature communications **8**, 14466 (2017).
[40] A. Damascelli, Z. Hussain, and Z.-X. Shen, Reviews of modern physics **75**, 473 (2003).